Research Square

Preprints are preliminary reports that have not undergone peer review.
They should not be considered conclusive, used to inform clinical practice,
or referenced by the media as validated information.

Deciphering ore genesis for auriferous deposits in Hangaliya area, Neoproterozoic Nubian Shield, Egypt: Emphasis on P-T conditions and ore-forming processes

Mohamed Abd El Monsef

monsef_egy@science.tanta.edu.eg

Tanta University

Ibrahim A. Salem

Tanta University

Gehad M. Saleh

Nuclear Materials Authority

Mohamed S. Kamar

Nuclear Materials Authority

Marek Slobodník

Masaryk University

Ahmed R. Hamad

Nuclear Materials Authority

Research Article

Keywords: Orogenic gold, geochemistry, EMPA, fluid inclusions, Nubian Shield (NS), Egypt

Posted Date: October 8th, 2026

DOI: https://doi.org/10.21203/rs.3.rs-11292804/v1

License: This work is licensed under a Creative Commons Attribution 4.0 International License.
Read Full License

Additional Declarations: No competing interests reported.

Abstract

The Hangaliya gold deposit in the South Eastern Desert (SED) of Egypt represents a characteristic example of an orogenic-type gold deposit within the Nubian Shield (NS). Nevertheless, the source of mineralizing fluids, ore genesis, and the deposit's evolutionary scenario within the broad tectonic framework of the Nubian shield remain unclear. A systematic integration between geology, geochemistry, mineralogy, and fluid inclusion studies has been applied to constrain contributions to the metallogenic processes for ore formation. The lode is confined to E-W and NE-SW auriferous quartz veins filling the fractures within granitic rocks. The host granitoid varies in composition from monzogranite to syenogranite, which displays I-type, alkaline nature, and typically developed in late to post-collisional tectonic settings. The paragenetic sequence for detected minerals can be divided into three stages: quartz + feldspar + pyrite (Py1) (Stage I); quartz + pyrite (Py2) + arsenopyrite + gold + chalcopyrite + sphalerite + pyrrhotite (Stage II); and goethite + covellite + sericite (Stage III). Two main types of primary fluid inclusions (FIs) are detected; namely Aqueous (H_2O±salt) and Mixed aqueous-carbonic (H_2O+CO_2±salt), the latter was subdivided into (two-phase inclusions & three-phase inclusions). The ore-forming fluids were predominantly derived from metamorphic sources generated through dehydration/decomposition processes. The estimated temperature of mineralization has been deduced in the range between 250 and 300°C; the obtained pressure varies from 0.7 to 1 Kbar. The gold-lode deposits at the Hangaliya area are supposed to be of orogenic-type, that share similar genetic aspects with other nearby gold deposits throughout the Nubian Shield.

1. Introduction

The Nubian Shield (NS) in Egypt is exposed in the Eastern Desert along the Red Sea coast for ≈800 km as length and extends downward, crossing the border with Sudan. The NS was considered as a north-left part of a large collision between the Arabian-Nubian Shield and the Mozambique Belt in East Africa, which is collectively together called "East African Orogen" (Stern, 1994). This orogenic collision had occurred when the East and West Gondwana were accidented to form the supercontinent named "Gondwana"; it was later on the closure of the Mozambique Ocean (~800–600 Ma) (Kroner, 1985; Stern, 1994; Loizenbauer et al., 2001) (Fig. 1). Such a great collision leads to the development of Pan-African Orogeny (PAO), which has been defined as a huge tectono-magmatic-metamorphic episode affecting the African continent near the end of the Neoproterozoic era, suggesting a time interval between (950-450 Ma) for this event (Kennedy, 1964). It was proposed that the cratonization of the NS had occurred ~570 Ma ago (El Gaby et al., 1988).

The NS of Egypt consists mainly of crystalline rocks (also called; basement rocks) that have been formed and developed in the Neoproterozoic era during the Pan-African Orogeny (PAO). These basement rocks in NS resemble a combination of island and continental arcs with their turbidities associated with subduction/obduction of the oceanic crust through tectonic suture and syn- to post-tectonic magmatic accretions in addition to molasse-type sediments (Hamimi et al., 2019). The formation of NS was inferred to three major stages of tectonic evolution: 1) Island arc stage (~870–635 Ma), recognized by

island arc volcano-sedimentary sequences, dismembered ophiolite suite, and metagabbro-diorite complex, (2) Collision/orogenic stage (~635–580 Ma), recognized by magmatic emplacement of I-type granites (tonalite, trondhjemite, and granodiorite), calc-alkaline granitic masses, and (3) Post-orogenic stage (590–540 Ma), characterized by an eruption and intrusion of fresh gabbroic rocks and alkaline to per-alkaline granitic plutons, the last two stages were accompanied by the development of sedimentary basins (Khalil et al., 2018 and references in). The Egyptian granitoids constitute about 57% of the total distribution for Neoproterozoic rocks of the NS in Egypt. They have been classified into two main groups; 1) syn- to late-orogenic/older granites, which are mostly of calc-alkaline type and display island arc tectonic settings in compressional regime (685-610 Ma: Stern and Hedge, 1985), and 2) post-to an-orogenic/younger granites with alkaline to peralkaline nature, which are mostly between volcanic-arc to intraplate tectonic settings related to extensional regime (600-475 Ma: Bentor, 1985; Stern and Hedge, 1985; Stern and Gottfried, 1986; Willis and Stern, 1988; Moghazi, 2003; Jarrar et al., 2003; Farahat et al., 2007; El Bahariya, 2021). In general, the granitic intrusions in NS of Egypt could be expressed as a series of arc-related to post-collisional to intraplate granitoid, involved in the transition from calc-alkaline I-type magma source to alkaline/peralkaline A-type protolith (e.g., El-Bialy, 2020; El Bahariya, 2021; Mokhtar et al., 2023).

The NS of Egypt has been considered as a mining district for gold in Africa with around 120 occurrences and/or deposits, mostly confined to the Neoproterozoic time. Mining workings were active through various periods started with Pharaonic (?), Predynastic times (3500 BCE), Old-Middle-New Kingdom (2700–1070 BCE), Greek-Ptolemaic-Roman-Byzantine (332 BCE–500 CE), Islamic (570 CE), and continued at different times in the Fifth (5th) Century and still up to now (over 6000 years of mining activities). The orogenic/mesothermal is the most common type of Egyptian gold rather than other genetic types (Intrusion/porphyry related-gold, VMS, BIF-associated gold, or placer deposits) (Fig. 2). In which the lode is restricted to auriferous quartz±carbonate veins dissecting the Neoproterozoic basement rocks of different lithologies (mainly granitoids). Most of the vein-type and dyke-type gold deposits are observed within/nearby granitic masses that seem to have had a significant role in gold precipitation. So, the possible genetic tie between the orogenic gold type and emplacement of granitic masses in NS is still a controversial matter. Some authors believe in the pure metamorphic model, in which the intrusion of granitic bodies was acting as the driving force required for circulation and enhancing the metamorphic process for mafic and/or ultramafic basement rocks. It leads to the leaching and liberation of gold and related metals from the hosting rocks (e.g., Hassaan and El-Mezayen, 1995; Hamdy and Aly, 2011). Others assume that the ascending magmatic fluids related to granitic intrusion have been contaminated with the metamorphic water during their passage, resulting in new hybrid mineralizing fluids with mixed compositions (magmatic-metamorphic parental fluids) (e.g., Botros, 2002, 2004; Surour et al., 1999; Abd El Monsef et al., 2018; Abd El Monsef, 2025).

The present study principally aims for better understanding of the source and genesis of gold and related metals in the Hangaliya area in view of the evolution of NS. As, Hangaliya is considered a role model for widespread orogenic/shear zone-related gold deposits in NS (especially those in the vicinity of granitic plutons). Geology, petrography, and geochemistry of the hosting granitic rocks have been

studied to delineate magma type and tectonic setting. Ore morphology, ore microscopy, and fluid inclusions for the gold deposits are also included in the current study to give a contribution on ore metallogeny and the physio-chemical conditions responsible for gold precipitation.

2. Geological and Structural Backgrounds

The studied area is covered by Neoproterozoic basement rocks exposed in G. Hafafit, G. Nugrus, G. Magal El Harami, and G. Hangaliya. The major Nugrus Thrust (Greiling et al., 1988) separates the rock units in the studied area into two distinct groups as follows: 1) Western group (named: Hafafit zone): it resembles the footwall of medium- to high-grade metamorphism, including mainly psammitic gneiss that is represented by Hafafit gneissic domes, and 2) Eastern group (named: Nugrus zone): it resembles the hanging wall of lower-grade metamorphism, including altered ultramafic rocks, serpentinites, and metagabbros. Both units were intruded by a series of late-to post-tectonic granitic masses of younger age. The main rock varieties can be arranged geochronologically (older to younger) as follows: ultramafics and related serpentinites, metagabbro, gneiss, monzogranite, and syenogranite. The ultramafic/serpentinite rocks occupy the northern part of the mappable area, which are found in different shapes and sizes, from boulders to blocks varying in size from a few meters to several meters of mountain block size. The textural and compositional variation of such rocks have been increased by alteration that was affected by serpentinization and carbonatization process. Metagabbros are dark, layered with low-medium relief; they, together with the ultramafic/serpentinite rocks, resemble a remnant of large masses of dismembered ophiolite succession. Gneisses occupy a huge part of G. Hafafit in the western-southern corner of the mapped area. These rocks are found in form of a core complex of gneissose domes that has been identified by El Gaby et al. (1990) as (infrastructure). They were over-thrusted by the ultramafic/serpentines and gabbroic rocks of (suprastructure) with tectonic contacts represented by low-angle thrust faults trending NW-SE and dipping 25º SW for about 16 km in length (Nugrus Thrust). Granitic rocks are in form of undeformed leucocratic type, they comprise monzo- to syeno-granites. These rocks are expressed as two large masses, namely the Nugrus and Magal El Harami granitoids, both plutons are found as NW-SE elongated bodies parallel to the same trend of the major Nugrus Thrust. The granites are massive, medium to coarse-grained, highly fractured, jointed and their color ranges from pink to buff and occasionally of a grayish appearance (Fig. 3).

Structurally, the area was clearly affected by intensive deformation and has apparently been subjected to extensional tectonic forces that led to the growing of fracture systems (plenty of faults, joints, and shear zones) cutting through the different rock units. Most of such fractures are filled with basic dykes, quartz veins/veinlets, and pegmatite bodies. The linear features and structural patterns have been automatically extracted as surface fractures based on Google Earth and multispectral aerial/satellite images of high spatial resolution using the software programme of LINDA (Masoud and Koike, 2017). The analysis of the automatically extracted lineament maps (Figs. 4a, b) exhibits the abundance of three main trend clusters in NNW-N, NE, and NEE directions associated with less dominant NNE-SSW, NW-SE, and E-W trends in for the depicted major lineaments. These results are summarized and expressed in the rose diagram and density stereogram for distribution, frequency, and number of lineaments (Fig. 4). In

the field, the faults are recorded in most rock units that are generally trending in the NNE-SSW and E-W directions; their lengths vary from 500 to 3500 m. Joints could be categorized as primary and secondary ones based on their origin. The first group of joints is confined to primary deformation through the early-formed rock units, mostly trending in the NNE-SSW direction. On the other hand, the second group of joints (i.e., secondary joints) are those that display a kinematic relation to local or regional structures (e.g., shear, fold, or fault), mostly trending in the NNW-SSE direction. Hagag et al. (2018) stated that the area was affected by sinistral transpressional-tectonic deformation, transposed many of the earlier formed structures into NNW or NW trends, and reflected the same trend of the well-known Najd Shear System along the NS of Egypt.

3. Sampling and analytical techniques

To fulfill all goals of the present study, we collected numerous numbers of samples from the (ore body, hosting granitic rocks and their accompanying alteration zone). The field study was supported by over 150 field photographs showing different rock varieties, morphology, field relationships, and structural features. The collected samples were examined in about 45 thin and thin-polished sections, using a transmitting and reflecting light microscope as a first step for mineral identification. About 100 microphotographs have been captured showing the rock-forming minerals, ore minerals, and the textural relations at the Petro. Lab. of the Nuclear Materials Authority (Egypt), and the ore minerals have been investigated at the Institute of Geological Sciences, Masaryk University (Czech Republic). Representative (19) samples from granitic rocks of G. Nugrus were subjected to whole-rock geochemical analyses of major oxides, trace elements, and REEs. The samples were investigated by X-ray fluorescence (XRF) measurements using the Supermini 200 Benchtop WDXRF Spectrometer by Rigaku at the Petroleum Research Institute, Cairo, Egypt. To confirm the previously identified ore minerals by ore microscopy, the economic minerals forming the ore body were investigated by Scanning Electron Microscope (SEM) equipped with an energy-dispersive spectrometer (EDS) unit (model version: Philips XL 30) at the laboratory of the Nuclear Materials Authority (Egypt). The operation conditions were used at 25–30 kV accelerating voltage, 1–2 mm beam diameter, and 60–120 seconds as counting time. Electron microprobe analysis (EMPA) has been applied in order to determine the elemental components found within the different ore minerals. This technique was carried out using a CAMECA SX-100 analyzer model attached with highly advanced spectrometers and detectors. The operating conditions applied for most minerals are 15 keV, 10 nA, and 2 μm as beam size. Pure and synthetic minerals were used as standards for the calibration process. These analyses were carried out at EMPA Lab., Institute of Geological Sciences, Masaryk University (Czech Republic). It is important to mention that the EMPA provides more accurate results than the standard SEM systems because of several factors, including the great sensitivity and high spectral resolution of the wavelength dispersive spectrometer (WDS), the analysis of light elements, and the detector dead time, which are much better than the Energy Dispersive Spectrometer (EDS). Fluid inclusions studies were accomplished using the LINKAM THSMG600 heating/freezing stage attached by the Pixelink digital camera for microphotographs. Synthetic fluid inclusions (i.e., H_2O-CO_2, H_2O-NaCl, and pure H_2O) were used for calibration of the stage. All

microthermometric measurements have been done at Fluid Inclusions' Lab. of the Institute of Geological Sciences, Masaryk University (Czech Republic). As normal procedures for microthermometry, we started with cooling down to -180°C with a cooling rate of 10°C/min with special care near specific temperatures (i.e., freezing temperatures). Then, we began to heat up with heating rates of 10°C/min that can be minimized to 1°C/min to record phases' changes below the temperature of 60°C, such as the melting temperature of solid CO_2 (Tm CO_2), the homogenization temperature of CO_2 (Th CO_2), the first melting of ice/eutectic temperature (Teu), the last melting of ice (Tm ice), the melting of clathrate/hydrated CO_2 (Tm clath), the temperature of total homogenization (Th total), and the decrepitation temperature (Td). Fluid compositions, molar volumes, fluid properties, and density-salinity calculations, as well as isochores constructions, were performed by the aid of the "FLUIDS" software package (Bakker, 2003).

4. Petrography and geochemistry of granitic rocks

Apparently, the granitic rocks in the area have different colors and compositions. Macroscopically, they are of medium to coarse grains, grey-reddish-grey to pink in color, and have a massive or occasionally pegmatitic appearance. They were examined under a microscope and have been classified petrographically into two categories of monzogranite and syenogranite as follows:

4.1. Petrography

Monzogranite is expressed in G. Nugrus of grey to pinkish-white color, it is composed mainly of K-feldspar quartz and biotite. The main accessory mineral represented by zircon and Fe-Mn oxides. Plagioclase represents about 40% of the total rock volume; it ranges in composition between albite and oligoclase (An_{16-18}). **Plagioclase** is found in form of subhedral to euhedral crystals exhibiting faint twining because of alteration to saussurite shreds. **K-feldspars** (30% of the total rock volume) are represented by perthite; it commonly exhibits distinct cross-hatching patterns. **Quartz** (25% of the total rock volume) either occurs as anhedral to subhedral crystals of medium-grained crystals or as interstitial fine grains filling the spaces between the other silicate minerals. **Biotite** forms lath-like crystals of euhedral to subhedral habit and characteristic pleochroism (straw yellow to brown). It is commonly altered to chlorite, epidote, and irregular patches of opaques; the alteration is usually visible along the crystal boundaries or through the cleavage plane. Occasionally, biotite crystals envelop some other accessory minerals, such as zircon that are sometimes surrounded by pleochroic halos (Fig. 5a).

Syenogranite forms the main component of Magal El Haram pluton, it is of medium to coarse-grained with a distinct equigranular texture and red to pinkish grey in color. It consists of K-feldspar (42%), quartz (40%), plagioclase (10%), biotite (5%) associated with epidote, sericite and carbonates, which are common secondary minerals. While, zircon, sphene and Fe-Mn oxides are the main accessories. **K-feldspars** are represented by microcline-microperthite and less common orthoclase-microperthite. They are obviously altered to sericite, carbonates, and less kaolinites. **Quartz** is either found as euhedral to subhedral large crystals/phenocrysts exhibiting wavy extinction or interstitially fills the interstices among the other constituents, or may corrode plagioclase, perthite and biotite. **Plagioclase** is of albite-

oligoclase (An_{9-28}) in composition. It occurs as subhedral prismatic or tabular crystals with lamellar twinging, the lamellae are obscured as they are partially or completely saussurized due to intensive alteration. **Biotite** is the common mafic mineral, it occurs as long and broad flakes (up to 2 mm in length & 1 mm in width) and generally encloses fine inclusions of quartz, zircon and Fe-Mn oxides. **Sphene** is recorded as equant/wedge-shaped crystals with euhedral to subhedral form associated with plagioclase, biotite, and k-felspars (Fig. 5b).

The modal analysis for the granite varieties was based upon the ratios of rock constituents in the investigated samples, through visual estimates using a point counter with a standard mechanical stage at the petrographic lab of the Nuclear Materials Authority, Egypt. The modal compositions inferred from the thin sections are plotted on the ternary classification diagram (Q-A-P) of (Streckeisen, 1976), it revealed that the studied granitoids are falling in the fields of monzogranite and syenogranite rocks (Fig. 5c).

4.2. Geochemistry

The studied granitic rocks have been subjected to geochemical analyses in order to clarify the geochemical characteristics, magma type and tectonic setting. This method helps for understanding the petrogenetic processes and evolution mechanism behind the emplacement of such granitic masses.

Based on petrographic investigation, nineteen samples have been selected and analyzed for their chemical components (i.e., Major oxides, normative compositions, trace elements and REEs) as shown in tables (1, 2). The provided data exhibits variations in the concentrations of major oxides and trace elements between syeno- and monzo-granites in the studied area. In general, there is an increase in the average contents of (K_2O, Na_2O, FeO^t, CaO) in syenogranite relative to their equivalent averages in monzogranite. However, a significant abundance for SiO_2 contents (Av.=73.81%) in monzogranite was observed compared to those in syenogranite (Av.=69.11%). Regarding trace elements, a remarkable increase was noticed in (Cr, Cu, Ni, Zr, Ga, Sr, Y, Rb) contents and a decrease in (V, Pb, Ba) contents between syenogranite and monzogranite.

The different geochemical relationships of major oxides and trace elements are the basic factors for nomenclature, classification, magma type and tectonic settings of the studied granitic rock units; Streckeisen (1976) established the normative Ab-Or-An ternary diagram to distinguish between different granitic varieties. The studied granite samples are scattered along the monzogranitic and syenogranitic fields (Fig. 6a). De La Roche et al. (1980) proposed a classification scheme to distinguish between plutonic igneous rocks based upon their cation proportions. Where the studied granitic samples are scattered along monzogranite and syenogranite fields (Fig. 6b). The magma types for the studied granitic rocks can be identified by using some discrimination diagrams. Hermes et al. (1978) used the molecular proportions of Al_2O_3-(Na_2O+K_2O)-CaO to differentiate between various magma types from which the rocks have been derived. The figure shows that the studied granitic rocks are of peraluminous nature (Fig. 6c). The Alkalinity ratio versus SiO_2 binary diagram was adopted by Wright (1969), which

differentiated between calc-alkaline, alkaline, and peralkaline granitic rock. Obviously, the studied samples are plotted into the alkaline field (Fig. 6d). The tectonic setting of the studied granitic rocks can be inferred using some binary diagrams, the SiO_2 against Al_2O_3 diagram (Maniar and Piccoli, 1989) reflecting that the granitic samples plot in the post-orogenic granitoids (POG) field (Fig. 7a). The Nb-Y diagram for the studied granitic rocks after (Pearce et al., 1984) revealed that the examined samples fall upon within-plate granitic field (WPG) (Fig. 7b). plotting the rock samples on the Y-Nb-3*Ga discrimination diagram of Eby (1992), it exhibits the post-collision setting for the studied granite rocks (Fig. 7c). On the Rb/Zr versus SiO_2 diagram (Harris et al., 1986), the studied granitoids plot in the field of I-type granites (Fig. 7d).

5. Deposits geology

The old Hangaliya gold mine has been exploited for gold since the early Pharaonic times. The styles of housing are ancient and modern, which could suggest that extraction of gold was not only confined to the present century but might date back to the Pharaonic and Roman times (Fig. 8a). Mining excavation was carried out through vertical and inclined shafts as well as open pits that represent the old surficial and underground working (Fig. 8b). The old mining activities, such as excavations, stopped-out quartz veins, tailings, dumps, and galleries are clearly observed throughout the mineralization area. Many ruins, which were used as dwellings for the workers, as well as archaic crushing tools are found near the Hangaliya gold mine site. These magnificent rudimentary tools consist mainly of large dense grinding stones (Fig. 8c). Production of gold at Hangaliya mine during this century was confined to the period between 1938 and 1952 (Mineral Map of Egypt, 1998).

The gold deposits at Hangaliya exhibit structural character related to faulting and fracturing that have been employed as a pathway for Au-rich hydrothermal fluids. The lode comprises a series of auriferous quartz veins, represented by three major veins with small branches and veinlets (namely, the 1^{st} vein, the 2^{nd} vein, and the 3^{rd} vein) (Fig. 9), showing significant potential for gold prospecting in the concealed parts of the ore district. The large areal extent of the gold mineralization in the area is related to (1^{st} vein & 2^{nd} vein), while recent exploration was recorded in quartz vein-3. The main vein (1^{st} vein) is trending in the E-W direction with a dipping of 70° N, its thickness up to 3 m along at which the main shafts of the Hangaliya gold mine were dug. The 2^{nd} vein is trending in the NE-SW direction with a dipping of 45° E; it has an average thickness of about one meter. However, the 3^{rd} vein is trending in the E-W direction with a dipping of 45° N with an average thickness of about 15 to 35 cm. It is milky-white in color with a reddish tint. The auriferous quartz veins are generally milky white, but sometimes they show shades of blue, green, and red coloration due to the intergrowth of azurite, chlorite, and goethite as secondary products of supergene alteration (Fig. 8d). Visible pyrite cubes and sulphide patches are observed in some samples from the area adjacent to the mineralized quartz veins (Fig. 8e).

The hydrothermal alteration in Hangaliya deposits primarily led to phyllic and argillaceous materials, which are primarily observed in close vicinity to gold mineralization during the main mineralization stage

(Fig. 10a,b). They are extensively developed along the contact between quartz veins and hosting granitic rocks, with variable width of the alteration zone ranging from few centimeters up to 70 cm. Phyllic alteration is characterized by replacement of primary felspar minerals with sericite, epidote, and pyrite with subordinate amounts of quartz (Fig. 10c). Argillic alteration is characterized by the production of a wide variety of soft clay minerals (i.e., kaolinite and illite) intercalated with quartz grains, commonly grayish in color and less friable than the surrounding fresh rocks (Fig. 10d). The presence of kaolinitic and sericitic alterations implies low pH conditions from 2 to 3 (acidic-leaching) at temperatures between 200 and 250ºC (Helgeson, 1974). Carbonatization and ferrugination are also recorded as remarkable signs of the late mineralization period.

6. Mineralogy

The ore is characterized by gold-bearing polymetallic sulphide-quartz veins. The most important ore minerals encountered in the studied quartz veins and alteration zones in the mine site are (gold, pyrite, chalcopyrite, sphalerite, galena, arsenopyrite, and pyrrhotite), as well as subordinate amounts of iron oxides.

The primary occurrence state of **gold** is the visible type, it occurs as fine minute specks scattered in the quartz vein, commonly within or nearby pyrite and/or arsenopyrite (Fig. 11a). **Pyrite** is the principal metallic mineral, which is represented in most of the studied samples. It is generally found as coarse-grained crystals (Py1) embedded within the large quartz crystals; most of the pyrite crystals are idiomorphic to subidiomorphic and mainly square-shaped grains (Fig. 11b). Some other pyrites (Py2) have smaller particle sizes (fine to medium-grained) and poorer crystal shape with sub- to anhedral crystal habit (Fig. 11c). The EMPA data differentiate between the two types of pyrites. Where Py1 exhibits higher contents of sulfur (51.78–53.15 wt.%) than those in Py2 (38.82–38.89) and lower amounts of iron (46.39–46.84 wt.%) than those in Py2 (59.27–59.4 wt.%) (Table 3). **Arsenopyrite** forms medium- to coarse-grained, euhedral crystals showing rhombic sections, rosettes, and cruciform crystals that are usually scattered in the groundmass or sometimes in attachment with pyrites (Fig. 11a,b,d,e). The composition of arsenopyrite comprises As contents variable from 38.61 to 41.31 wt.%, Fe (35.62–36.48 wt.%), and S (22.11–24.51 wt.%) (Table 3). **Chalcopyrite** is found to be fine-grained of anhedral aggregates scattered within quartz groundmass (Fig. 11d). Infrequently, chalcopyrite crystals are partially altered to covellite along the periphery, showing the characteristic blue color with strong pleochroism forming a rim replacement texture (Fig. 11f). **Sphalerite** occurs in form of fine-grained anhedral aggregates included in large pyrite crystals. It is characterized by a light grey color and medium reflection (Fig. 11c). **Pyrrhotite** is detected as fine anhedral aggregates involved in large pyrite crystals (Fig. 11g). It is characterized by a light brown color and weak pleochroism. **Iron oxides** are almost altered to goethite except for small relics of anhedral grains scattered in the groundmass, sometimes goethite may completely replace pyrite (replacement texture) or be found along the periphery of other main sulphide minerals (Fig. 11h).

The mineral paragenesis of Hangaliya gold deposit is determined on the basis of the petrographic overgrowth, replacement textures ore and structures displayed through the ore minerals and their altered products. It has been established that the formation of the Hangaliya Au-deposit can be divided into three recognized stages. These stages are (from early to late, as follows, Table 4): quartz + feldspar + Py1 (Stage I); quartz + Py2 + arsenopyrite + gold + chalcopyrite + sphalerite + pyrrhotite (Stage II); and goethite + covellite + sericite (Stage III).

7. Fluid Inclusions (FIs)

7.1. Types and characteristics of fluid inclusions

The fluid inclusions (FIs) in quartz crystals are common and show large variation in shape and size. They are more abundant in less-deformed quartz crystals than in the others of the studied veins, as the quartz is clearer and more transparent. Based on detailed petrographic observations by Roedder (1984), combined with the transition of FIs during thermal cycling (heating and freezing behavior), two main compositional types of fluid inclusions can be recognized as follows:

1) Aqueous type (H_2O±salt): The aqueous inclusions can be easily identified by their relatively transparent color and homogenization temperatures, predominantly higher than 100°C. These inclusions contain two visible phases at room temperature in the form of an outer aqueous liquid phase and an inner small aqueous-vapor bubble (Fig. 12a). They resemble about 40% of the total number of detected FIs at room temperature. The FIs occur in form of small, isolated inclusions within quartz crystals of primary origin or lie along healed microfractures as arrays (trials) cross-cutting quartz boundaries of undoubted secondary nature. In shape, they always exhibit irregular or elongated shapes and sometimes equate-shaped inclusions of euhedral faces (negative crystals). Their sizes range from 9 to 19 μm and have a degree of fill between 0.95 and 0.85 vol.% liquid.

2) Mixed aqueous-carbonic type (H_2O+CO_2±salt): They are commonly isolated with no planar array and typically display a regular shape, suggesting a primary origin. They can be further divided into two forms based on the number of phases at room temperature (two-phase and three-phase FIs) as follows: *i) two-phase inclusions;* they contain two main phases at room temperature in form of an inner carbonic vapor bubble and an outer aqueous liquid phase. The boundary between the two phases is always dark and bold, probably due to the presence of an invisible thin layer of carbonic liquid phase between the two main visible phases. They resemble about 20% of all detected FIs at room temperature. The FIs are commonly found in the form of isolated inclusion of primary origin. Generally, this type of FIs ranges in size between 9 and 17 μm. Regarding the shape, they are mostly found in form of tabular or rhombohedral inclusions (Fig. 12b). *ii) three-phase inclusions:* the FIs are characterized by the presence of three visible phases at room temperature, as an outer aqueous liquid phase, which is going inward by a carbonic liquid phase, and a more inner carbonic vapor bubble (Fig. 12c). The carbonic-liquid phase is generally darker than the aqueous phase at room temperature. This type is probably of primary origin and occurs as isolated inclusions ranging from 8 to 17 μm in size, they resemble about 35% of all

detected FIs at room temperature. Monophase FIs have also been detected in form of pure liquid inclusion and pure vapor inclusion; these inclusions exhibit anhedral to subhedral oval-shaped crystals (Fig. 12b). The existence of the monophase type of FIs was probably referred to the distillation process for the primary FIs types.

7.2. Fluid inclusions' microthermometry results

This technique is valuable for discovering the temperatures at which the hosting minerals have been grown. Through the cooling-heating regime, several temperatures were recorded as follows: Freezing temperature of water (Tf H_2O), melting temperatures of solid CO_2 (Tm CO_2), melting of ice (Tm ice), melting of clathrate (Tm clath), homogenization temperatures of CO_2 (Th CO_2), and total homogenization temperature (Th total) were measured for the studied fluid inclusions. Salinity, density, and mole fractions were calculated using the BULK fluid inclusion program, version 01/03 of Bakker (2003). Salinities were expressed as weight percent equivalent of NaCl (NaCl equi) based upon (Tm ice) for aqueous types of FIs. In the mixed aqueous-carbonic type, (Tm clath) accompanied by (Tm ice) are used to obtain the salinity of this type of FIs. Density and amount of substance fractions were determined using the (Zhang and Frantz, 1987) equation of state. Densities were expressed by (g/cm³). The microthermometric data and calculated parameters for FIs of measured aqueous and aqueous-carbonic types are summarized in Table (5).

1) Aqueous type (H_2O±salt): Two groups of fluid inclusions were distinguished based on the nature of inclusions, occurrences, and homogenization temperatures: primary and secondary fluid inclusions. During cooling, the primary aqueous FIs display a freezing temperature of water for (Tf H_2O) ranging from -36.3 to -44.8°C with an average of -39.7°C. Ice-melting temperature (Tm ice) varies between -3.1 and -1.5°C, averaging -2.27°C. The total homogenization temperature (Th total) ranges from 215 to 266°C with an average of 255.67°C. Bulk density is in the range of 0.86–0.89 g/cm³, with a mean value of 0.88 g/cm³. The total salinity has a range from 2.45 to 4.93 wt.% of NaCl with an average of 3.7 wt.% of NaCl equivalent. The secondary aqueous FIs values, on the other hand, are characterized by lower (Th total), which range from 114 to 155°C and average 135.63°C. The (Tf H_2O) extends from -37 to -43.2°C with an average of -40.56°C. While the (Tm ice) has a range of (-2.7 & -1.2°C), averaging -2.05°C. Bulk densities vary in range (0.94–0.97 g/cm³) with a mean value of 0.95 g/cm³. Total salinity has a range from 2.07 to 4.49 wt.% of NaCl with an average of 3.45 wt.% of NaCl equivalent.

2) Mixed aqueous-carbonic type (H_2O+CO_2±salt): *i) Two-phase inclusions*; the melting temperature of CO_2 (Tm CO_2) ranges from -57 to -56.6°C with an average of -56.74°C. The melting temperature of ice (Tm ice) has a range from -5.3 to -3.7°C with an average of -4.64°C. The melting temperature of clathrate (Tm clath) ranges from 5.8 to 7.2°C, with an average of 6.45°C. They always exhibit relatively high temperature at total homogenization relative to pure aqueous inclusions with a range between 306 and 345°C and an average of 331.26°C; the higher (Th total) is probably due to the presence of the CO_2 component within the system. Bulk density ranges from 0.66 to 0.77 g/cm³, with a median of 0.68 g/cm³. Total salinity ranges between 6.08 and 8.39 wt.% of NaCl equi., with an average of 7.62 wt.% of

NaCl. Fluid inclusions of this type are always higher in salinity than those belonging to aqueous inclusions due to the effect of CO_2 molecules. Aqueous volume percentage ranges from 60 to 70% relative to the total volumes of inclusions, with a median of 63.5%. These inclusions show relatively low content of carbonic fractions with a range of 0.028–0.036 mole fractions with a median of 0.033 and high content of water moves with a total range of 0.92 to 0.94 mole fractions and a median of 0.92 mole fractions, so it could be described as water-rich FIs (high H_2O content). *ii) Three-phase inclusions:* the melting temperature of CO_2 (Tm CO_2) ranges from -57 to -56.6°C, averaging -56.83°C. Ice-melting temperature (Tm ice) varies from -5.4 to -3.3°C with an average of -4.9°C. The melting temperature of clathrate (Tm clath) ranges from 5.6 to 9.6°C, with an average of 7.46°C. The temperature of homogenization for CO_2 (Th CO_2) extends between 28 and 30.1°C with an average of 29.36°C; most of them were homogenized to the liquid state, and the others were homogenized to the vapor state and rarely to the critical state (through fading of the meniscus). The total homogenization temperature (Th total) ranges from 253 to 395°C with an average of 344°C. Most of the inclusions were totally homogenized to the liquid state with the disappearance of the vapor bubble before decrepitating. Bulk density has a range between 0.67 and 0.78 g/cm³ with a median of 0.73 g/cm³. Total salinity has a range between 5.47 and 8.53 wt.% of NaCl equi., with an average of 8.18 wt.% of NaCl. Aqueous percentage displays a range between 10 and 30% of the total volume. These inclusions show relatively higher content of carbonic fractions with a range of 0.50 to 0.88 mole fractions with a median of 0.63 and lower content of water moves with a total range of 0.08 to 0.48 mole fractions and a median of 0.25 mole fractions, so it could be described as carbon-rich FIs.

8. Discussion

8.1. Nature and evolution of Au-forming fluids

Generally, the fluid inclusions (especially primary ones) in hydrothermal system can preserve a critical record of physicochemical conditions at which the hosting mineral was crystallized. Most of the FIs at Hangaliya deposits are apparently distributed within quartz crystals, which are inferred to be of the primary type. In contrast, other inclusions, especially those related to the aqueous type, lie along healed microfractures and are clearly of secondary origin, which refers to formation in later stages not related to either quartz solidification or the mineralization process. Histograms of fluid inclusions data for different fluid systems from the auriferous quartz vein are shown in Fig. 13a. The diagram distinguishes between two peaks of different clusters at 140 & 240°C, representing primary and secondary aqueous FIs. However, the aqueous-carbonic FIs show a single peak for the cluster around 350°C. The coexistence of different types and subtypes of primary fluid inclusions in any given gold deposits may refer to continuous fluid evolution during heterogeneous trapping (Neumayr & Hagemann, 2002). Using the available data for construction of a binary diagram between (salinity versus total homogenization temperature) for all types of FIs. It shows a general evolutionary trend reflecting the sign of isothermal mixing of two immiscible fluids in the given medium (Wilkinson, 2001) (Fig. 13b). Therefore, we suggest that the originally high-temperature ore fluid was later contaminated with another lower-temperature water during fluid uplifting. However, there is a noticeable variation in the CO_2 content ranging from

carbon-rich inclusions to dominant aqueous fluids without a carbonic phase. The presence of water-rich and carbonic-rich fluid inclusions suggests that the water was saturated with carbon when the auriferous quartz veins had been formed (Mullis, 1979). The presence of carbonic-rich fluid inclusions with a maximum temperature of homogenization (395°C), the absence of any solid phase of salts or daughter minerals within fluids, as well as low to medium salinities of all types of FIs (up to 8.53 wt.% of NaCl equi.), and all criteria are consistent with the fact that the ore-forming fluids were generated from a metamorphic source with a reasonable possibility of subsequent mixing with later surface/meteoric water (Fig. 13b).

Based on petrographic characteristics and microthermometric measurements or FIs, two stages of fluid formation were recognized in the study area: the first stage (mineralizing stage) that is characterized by the formation of low-density aqueous-carbonic fluid inclusions with a high hominization temperature (306 to 395°C) accompanied by the formation of primary aqueous inclusions at a relatively moderate temperature (215 to 266°C). The presence of these two types in the same field of view next to each other in form of colonies could be interpreted as that the primary aqueous inclusions were formed through leakage of pure water phase from the previously-formed aqueous-carbonic inclusions with decreasing of temperature (retrograde). The second stage of fluid formation is referred to secondary aqueous FIs occurring at low temperature (114 to 155°C), that have been developed through fractures and cracks cross-cutting the pre-existed auriferous quartz veins. The secondary fluid inclusions were formed in later stage and have no link with mineralization events.

8.2. P-T conditions of mineralization

For any given solution, when it starts to boil and evaporate, it splits into two coexisting separated phases: a liquid phase and another vapor phase with random proportions of those two phases. The presence of different types of fluid inclusions with varying degrees of fill (relative ratio between fluid and vapor phases) may suggest a synchronous entrapment through boiling/effervescence conditions (phase separation) from a hot solution (Van den Kerkhof and Hein, 2001). In such an environment, the estimation of trapping conditions of fluids (i.e., P-T conditions) permits reliable information for the ore-forming conditions (Roedder and Bodnar, 1980). Where the homogenization temperatures can directly refer to the entrapment temperature of fluids, and the pressure can be determined through the combining isochores of FIs with different compositions covering the minimum and maximum densities (Roedder and Bodnar, 1980; Van den Kerkhof and Hein, 2001). Based on the isochores calculations for different fluid inclusion types (primary aqueous and aqueous-carbonic inclusions), the detected temperature of mineralization was in the range of 250 to 300ºC, and the obtained pressure is between 0.7 and 1 Kbar (Fig. 13c).

The trigger mechanisms for ore deposition started with fluid immiscibility, followed by heterogeneous trapping, fluid mixing, cooling, and pressure drop through fluid circulation/upwelling, and finally ended with fluid-wall-rock reactions. Among these processes, cooling and fluid–wallrock reactions appear to

have been the principal factors that created the suitable medium and conditions favorable for mineral deposition during ore precipitation.

8.2. Geodynamic setting and genetic type

Most of the worldwide lode-gold deposits were considered to be of the orogenic type, in addition to other less distributed intrusion-related/porphyry gold systems, VMS-related gold, skarn and Carlin-type deposits, as well as Au-deposits related to weathering and supergene processes (e.g., placer deposits). The typical "orogenic gold deposits" are described as being vein-type, structurally controlled, mesothermal, and greenstone-hosted gold deposits. They are commonly associated with compressional/transpressional tectonic regimes at a long convergent plate margin during accretionary and collisional orogenesis and commonly correspond to syn- to late metamorphic events (Groves et al., 1998; Abd El-Wahed 2025). In Egypt, a spatial-temporal relationship is remarkable between gold mineralization and shear zones intersecting ophiolitic arc assemblages and late-orogenic granitoids (Abd El Monsef et al., 2018; Abd El Monsef and Abdelnasser, 2021).

Based on the geologic-tectonic settings, mineralogy, and fluid inclusion data, several pieces of evidence strengthen an orogenic type of Hangaliya gold deposit, among them (1) the deposits are of vein-type that are clearly of structural control, the gold-lode is confined to fissure-filling quartz veins extending E-W and NE-SW directions, and the ore orientation revealed that the deposition was post-dated the well-known Najd Shear System (NW) that controls the major trends and emplacement of different rock units in the study area. (2) The auriferous veins are confined to granitic rocks (monzogranite and syenogranite), which exhibit I-type alkaline characteristics related to late to post-collisional tectonic settings. The intrusion of granitic masses within the shear zone probably played an important role as a heat engine to facilitate and accelerate the circulation of hydrothermal water through ore deposition. Another study supposes that due to the low-tensile strength of solid granitic rocks relative to neighbor units, it released a favorable trap zone that influenced the creation of a structural framework for fluid migration and deposition (Botros, 2015; Zoheir et al., 2018; Abd El Monsef, 2025). (3) The majority of lithos in the whole area are of metamorphic rocks related to green schist to amphibolite facies (i.e., gneiss, ultramafic/serpentinite rocks, and metagabbro). We suppose that the gold has been sourced from a basic source (ultramafic/serpentinite & gabbroic rocks) through metamorphic episodes during the orogeny; such an assumption was supported by data from a fluid inclusions study. (4) The diversity of wallrock alteration types (i.e., phyllic and argillic alterations), which closely resembles to other alteration facies documented at the nearby orogenic-gold localities in the Nubian shield including; El Sid (Zoheir and Moritz, 2014), Dungash (Salem et al., 2016), Gidami (Abd El Monsef et al., 2018), and Atalla (Abd El Monsef, 2020). (5) The isochores calculations revealed P-T conditions in a range of (T=250–300ºC & P=0.7–1 Kbar), corresponding to the mesothermal/orogenic type of deposits.

References

1. Abd El Monsef, M. (2020). Ore Controls and Metallogenesis of Au-Ag Deposits at Atalla Mine, Central Eastern Desert of Egypt. *Acta Geologica Sinica-English Edition*, 94(5), 1451-1470.
2. Abd El Monsef, M. (2025). An Overview for Gold Mineralization in the Egyptian Segment of the Northern Continuation of the East African Orogen. In: Hamimi, Z., et al. Gold Deposits in Egypt. *Sustainable Landscape Planning and Natural Resources Management. Springer, Cham*.
3. Abd El Monsef, M., & Abdelnasser, A. (2021). Ore-forming mechanism and its relationship with deformational and metamorphic episodes at Haimur gold mine, Nubian Shield, Egypt. *Geological Magazine*, 158(3), 518-536.
4. Abd El Monsef, M., Slobodnik, M. and Salem, I. A. (2018): Hydrothermal evolution of granitoid-hosted gold mineralization in Gidami area: an example for orogenic-gold deposits in Egypt. *Journal of African Earth Science*, 146, P. 132-149.
5. Abd El Monsef, M., Slobodník, M., & Salem, I. A. (2018). Hydrothermal evolution of granitoid-hosted gold mineralization in gidami area: An example for orogenic-gold deposits in Egypt. *Journal of African Earth Sciences*, 146, 132-149.
6. Abd El-Wahed, M. A. (2025). Shear-related gold mineralization in the Egyptian Nubian Shield, East African orogenic belt. *Mediterranean Geoscience Reviews*, 7(2), 185-253.
7. Bakker, R. J. (2003). Package FLUIDS 1. Computer programs for analysis of fluid inclusion data and for modelling bulk fluid properties. *Chemical Geology*, 194(1-3), 3-23.
8. Bentor, Y. K. (1985). The crustal evolution of the Arabo-Nubian Massif with special reference to the Sinai Peninsula. *Precambrian research*, 28(1), 1-74.
9. Bodnar, R. J. (1993). Revised equation and table for determining the freezing point depression of H_2O-NaCl solutions. *Geochimica et Cosmochimica acta*, 57(3), 683-684.
10. Botros, N. S. (2002): Alteration zones: Are they a good target for gold deposits in Egypt?" *Arab Gulf Journal of Scientific Research* 20 (2002): 209-218.
11. Botros, N. S. (2004). A new classification of the gold deposits of Egypt. *Ore Geology Reviews*, *25*(1-2), 1-37.
12. Botros, N. S. (2015). The role of the granite emplacement and structural setting on the genesis of gold mineralization in Egypt. *Ore Geology Reviews*, 70, 173-187.
13. De la Roche, H. D., Leterrier, J. T., Grandclaude, P., & Marchal, M. (1980). A classification of volcanic and plutonic rocks using R1R2-diagram and major-element analyses—its relationships with current nomenclature. *Chemical geology*, *29*(1-4), 183-210.
14. Eby, G. N. (1992). Chemical subdivision of the A-type granitoids: petrogenetic and tectonic implications. *Geology*, 20(7), 641-644.
15. EGSMA (1998) Metallogenic Map of Arab Republic of Egypt, Metallic Ores and NonMetallic Deposits, Scale 1:1,000,000. *Egyptian Geological Survey and Mining Authority*. Exploration sheet.
16. El Bahariya, G. A. (2021). *An overview on the classification and tectonic setting of Neoproterozoic granites of the Nubian Shield, Eastern Desert, Egypt*. IntechOpen.

17. El Bialy, M. Z. (2020): Precambrian Basement Complex of Egypt. In: Hamimi, Z. El-Barkooky, A., Martínez Frías, J., Fritz, H. and Abd El Rahman, Y., The Geology of Egypt, *Regional Geology Reviews*, Springer Nature Switzerland, P. 81-129.
18. El-Gaby, S., List, F. K., & Tehrani, R. (1988). Geology, evolution and metallogenesis of the Pan-African belt in Egypt. In *the Pan-African belt of Northeast Africa and adjacent areas: tectonic evolution and economic aspects of a late proterozoic Oregon* (pp. 17-68).
19. Farahat, E. S., Mohamed, H. A., Ahmed, A. F., & El Mahallawi, M. M. (2007). Origin of I-and A-type granitoids from the Eastern Desert of Egypt: implications for crustal growth in the northern Arabian–Nubian Shield. *Journal of African Earth Sciences*, 49(1-2), 43-58.
20. Gehrig, M. (1980). Phasengleichgewichte und PVT-Daten ternarer Mischungen aus Wasser, Kohlendioxid und Natriumclorid bis 3 kbar und 550°C. *Ph. D. Thesis, University Karlsruhe, Hochschulverlag, Freiberg, Germany*, 212 pp.
21. Gray, D. R., Foster, D. A., Maas, R., Spaggiari, C. V., Gregory, R. T., Goscombe, B., & Hoffmann, K. C. (2007). Continental growth and recycling by accretion of deformed turbidite fans and remnant ocean basins: Examples from Neoproterozoic and Phanerozoic orogens.
22. Greiling, R. O., El Ramly, M. F., El Akhal, H., & Stern, R. J. (1988). Tectonic evolution of the northwestern Red Sea margin as related to basement structure. *Tectonophysics*, 153(1-4), 179-191.
23. Groves, D. I., Goldfarb, R. J., Gebre-Mariam, M., Hagemann, S. G., & Robert, F. (1998). Orogenic gold deposits: a proposed classification in the context of their crustal distribution and relationship to other gold deposit types. *Ore geology reviews*, 13(1-5), 7-27.
24. Hagag, W., Moustafa, R., & Hamimi, Z. (2018). Neoproterozoic Evolution and Najd—Related Transpressive Shear Deformations Along Nugrus Shear Zone, South Eastern Desert, Egypt (Implications from Field—Structural Data and AMS—Technique). *Geotectonics*, 52(1), 114-133.
25. Hamdy, M. M., & Aly, G. A. (2011). Preliminary results of a first record of gold and uranium in marble from Central Eastern Desert, Egypt: a witness for (syn-and post-?) metamorphic mineralization in metasediments. *Arabian Journal of Geosciences*, 4(1), 25-43.
26. Hamimi, Z., Abd El-Wahed, M. A., Gahlan, H. A. and Kamh, S. Z. (2019): Tectonics of the Eastern Desert of Egypt: Key to understanding the Neoproterozoic evolution of the Arabian-Nubian Shield (East African Orogen). In: Bendaoud, A., Hamimi, Z., Hamoudi, M., Djemai, S. and Zoheir, B. (Eds.), Geology of the Arab World- An Overview, *Springer Geology*, P. 1-81.
27. Harris, N. B. W., Pearce, J. A. and Tindle, A. G., (1986): Geochemical characteristics of collision-zone magmatism. In: M. P. Coward and A. C. Ries (eds.): *Collision Tectonics*, P. 67-81, Blackwell, Oxford.
28. Hassaan, M. M. (1995). Genesis of gold mineralization in Eastern Desert, Egypt. *Al-Azhar Bull. Sci.*, *6*, 921-939.
29. Helgeson, H. C. (1979). Chemical interaction of feldspars and aqueous solutions. *The Feldspars*, 184-217.
30. Hilmy, M. E., & Osman, A. (1989). Remobilization of gold from a chalcopyrite-pyrite mineralization Hamash gold mine, Southeastern Desert, Egypt. *Mineralium Deposita,* 24(4), 244-249.

31. Hermes, O. D., Ballard, R. D., & Banks, P. O. (1978). Upper Ordovician peralkalic granites from the Gulf of Maine. *Geological Society of America Bulletin*, *89*(12), 1761-1774.
32. Jarrar, G., Stern, R. J., Saffarini, G., & Al-Zubi, H. (2003). Late-and post-orogenic Neoproterozoic intrusions of Jordan: implications for crustal growth in the northernmost segment of the East African Orogen. *Precambrian research*, *123*(2-4), 295-319.
33. Kennedy, W. Q. (1964). The structural differentiation of Africa in the Pan-Africa (±500 my) tectonic episode. *Univ, Leeds, Res. Inst. African Geol., Ann. Rept.*, 48-49.
34. Khalil, A. E. S., Obeid, M. A., Azer, M. K., & Asimow, P. D. (2018). Geochemistry and petrogenesis of post-collisional alkaline and peralkaline granites of the Arabian-Nubian Shield: a case study from the southern tip of Sinai Peninsula, Egypt. *International Geology Review*, *60*(8), 998-1018.
35. Kröner, A. (1985). Ophiolites and the evolution of tectonic boundaries in the late proterozoic Arabian—Nubian shield of northeast Africa and Arabia. *Precambrian Research*, *27*(1-3), 277-300.
36. Loizenbauer, J., Wallbrecher, E., Fritz, H., Neumayr, P., Khudeir, A. A., & Kloetzli, U. (2001). Structural geology, single zircon ages and fluid inclusion studies of the Meatiq metamorphic core complex: implications for Neoproterozoic tectonics in the Eastern Desert of Egypt. *Precambrian Research,* 110(1-4), 357-383.
37. Maniar, P. D., & Piccoli, P. M. (1989). Tectonic discrimination of granitoids. *Geological society of America bulletin*, *101*(5), 635-643.
38. Masoud, A., & Koike, K. (2017). Applicability of computer-aided comprehensive tool (LINDA: LINeament Detection and Analysis) and shaded digital elevation model for characterizing and interpreting morphotectonic features from lineaments. *Computers & Geosciences*, 106, 89-100.
39. Moghazi, A. M. (2003). Geochemistry and petrogenesis of a high-K calc-alkaline Dokhan Volcanic suite, South Safaga area, Egypt: the role of late Neoproterozoic crustal extension. *Precambrian Research*, *125*(1-2), 161-178.
40. Mokhtar, H., Surour, A. A., Azer, M. K., Ren, M., & Said, A. (2023). Petrogenesis and possible fingerprints of the Najd shear system on the evolution of deformed granitic rocks in the west Wadi Nugrus area, Egypt. *Journal of African Earth Sciences*, 207, 105045.
41. Mullis, J. (1979). The system methane-water as a geologic thermometer and barometer from the external part of the Central Alps. *Bulletin de Minéralogie*, 102(5), 526-536.
42. Neumayr, P., & Hagemann, S. G. (2002). Hydrothermal fluid evolution within the Cadillac tectonic zone, Abitibi greenstone belt, Canada: relationship to auriferous fluids in adjacent second-and third-order shear zones. *Economic Geology*, 97(6), 1203-1225.
43. Pearce, J. A., Harris, N. B., & Tindle, A. G. (1984). Trace element discrimination diagrams for the tectonic interpretation of granitic rocks. *Journal of petrology*, *25*(4), 956-983.
44. Roedder, E. (1984). Volume 12: fluid inclusions. Rev. Mineral, 12, 644.
45. Roedder, E., & Bodnar, R. J. (1980). Geologic pressure determinations from fluid inclusion studies. *Annual Review of Earth and Planetary Sciences*, Vol. 8, p. 263, 8, 263.

46. Salem, S. M., El Sharkawi, M., El-Alfy, Z., Soliman, N. M., & Ahmed, S. E. (2016). Exploration of gold occurrences in alteration zones at Dungash district, Southeastern Desert of Egypt using ASTER data and geochemical analyses. *Journal of African Earth Sciences*, 117, 389-400.
47. Stern, R. J. (1994). Arc assembly and continental collision in the Neoproterozoic East African Orogen: implications for the consolidation of Gondwanaland. *Annual review of earth and planetary sciences*, 22(1), 319-351.
48. Stern, R. J. and Gottfried, D. (1986): Petrogenesis of late Precambrian (575–600 Ma) bimodal suite in north-east Africa. *Contributions to Mineralogy and Petrology,* 92, P. 492-501.
49. Stern, R. J., & Hedge, C. E. (1985). Geochronologic and isotopic constraints on late Precambrian crustal evolution in the Eastern Desert of Egypt. *American Journal of Science*, *285*(2).
50. Streckeisen, A. (1976). To each plutonic rock its proper name. *Earth-science reviews*, *12*(1), 1-33.
51. Surour, A. A., Attawiya, M. Y., Hussein, H. A., & El-Feky, M. G. (1999). Shear zone microfabrics and multiple source of gold at the Hangaliya Mine, Eastern Desert, Egypt. *The Journal of Geology*, *43*, 39-52.
52. Surour, A. A., El-Bayoumi, R. M., Attawiya, M. Y., & El-Feky, M. G. (2001). Geochemistry of wall rock alterations and radioactive mineralization in the vicinity of Hangaliya uraniferous shear zone, Eastern Desert, Egypt. *Egyptian Journal of Geology,* 45(1), 187-212.
53. Van den Kerkhof, A. M., & Hein, U. F. (2001). Fluid inclusion petrography. *Lithos*, 55(1-4), 27-47.
54. Wilkinson, J. J. (2001). Fluid inclusions in hydrothermal ore deposits. *Lithos*, 55(1-4), 229-272.
55. Willis, K. M., Stern, R. J., & Clauer, N. (1988). Age and geochemistry of Late Precambrian sediments of the Hammamat Series from the Northeastern Desert of Egypt. *Precambrian Research*, *42*(1-2), 173-187.
56. Wright, J. B. (1969). A simple alkalinity ratio and its application to questions of non-orogenic granite genesis. *Geological Magazine*, *106*(4), 370-384.
57. Zhang, Y. G., & Frantz, J. D. (1987). Determination of the homogenization temperatures and densities of supercritical fluids in the system NaClKClCaCl2H2O using synthetic fluid inclusions. *Chemical Geology*, 64(3-4), 335-350.
58. Zoheir, B., & Moritz, R. (2014). Fluid evolution in the El-Sid gold deposit, Eastern Desert, Egypt. *Geological Society Special Publication*, *402*(1), 147-175.
59. Zoheir, B., Deshesh, F., Broman, C., Pitcairn, I., El-Metwally, A., & Mashaal, S. (2018). Granitoid-associated gold mineralization in Egypt: a case study from the Atalla mine. *Mineralium Deposita*, 53(5), 701-720.

Tables

Table 1 to 5 are available in the Supplementary Files section.

Figures

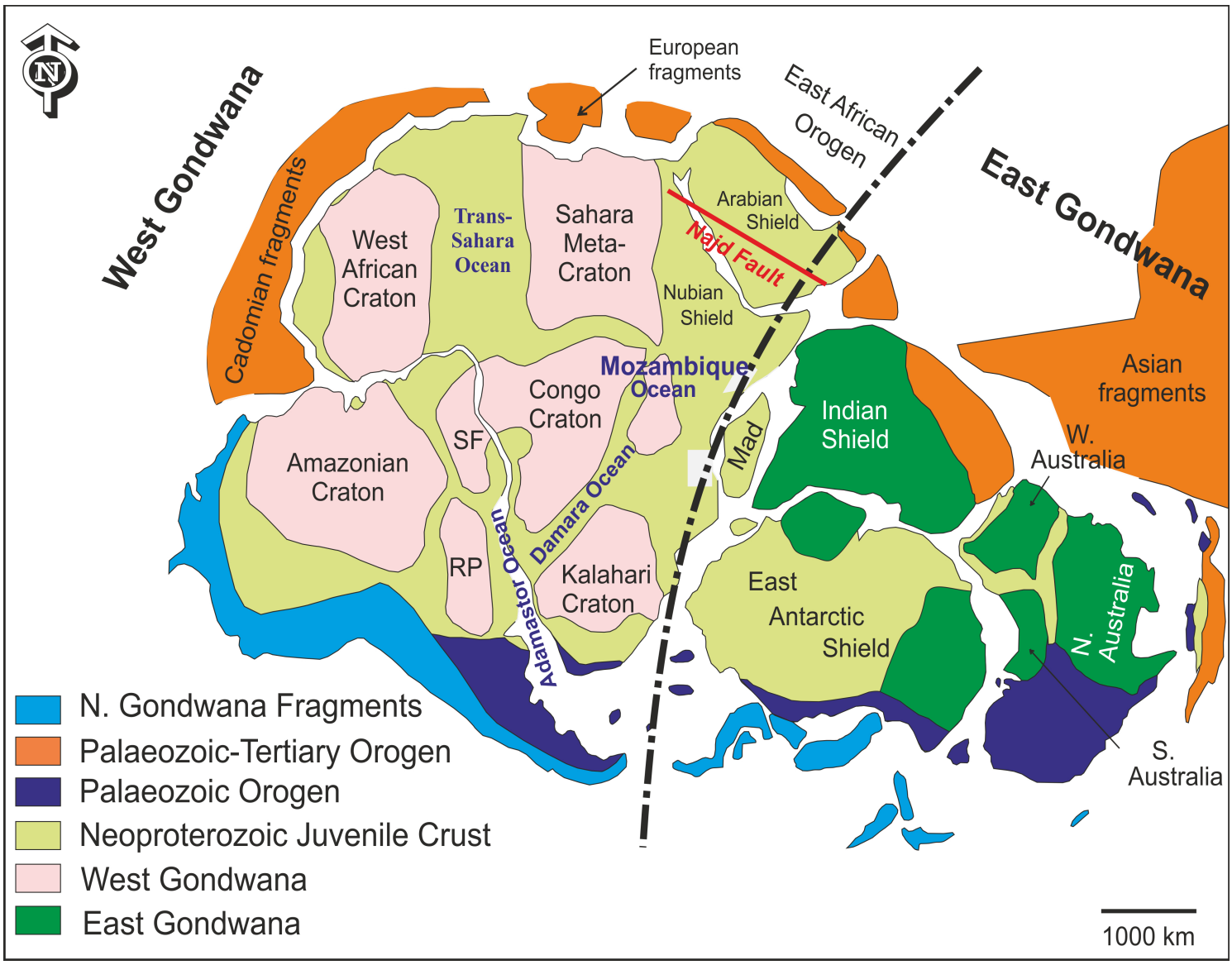


Figure 1

Amalgamation of West and East Gondwana showing the paleo-position of the Arabian-Nubian Shield (ANS) during the Neoproterozoic era (Gray et al., 2007).



Figure 2

The distribution of the most common genetic-types of gold deposits in Egypt accompanied by major tectonic structure (fault and shear belts) (Hilmy et al, 1989), with referring to the Hangaliya deposits (study area).

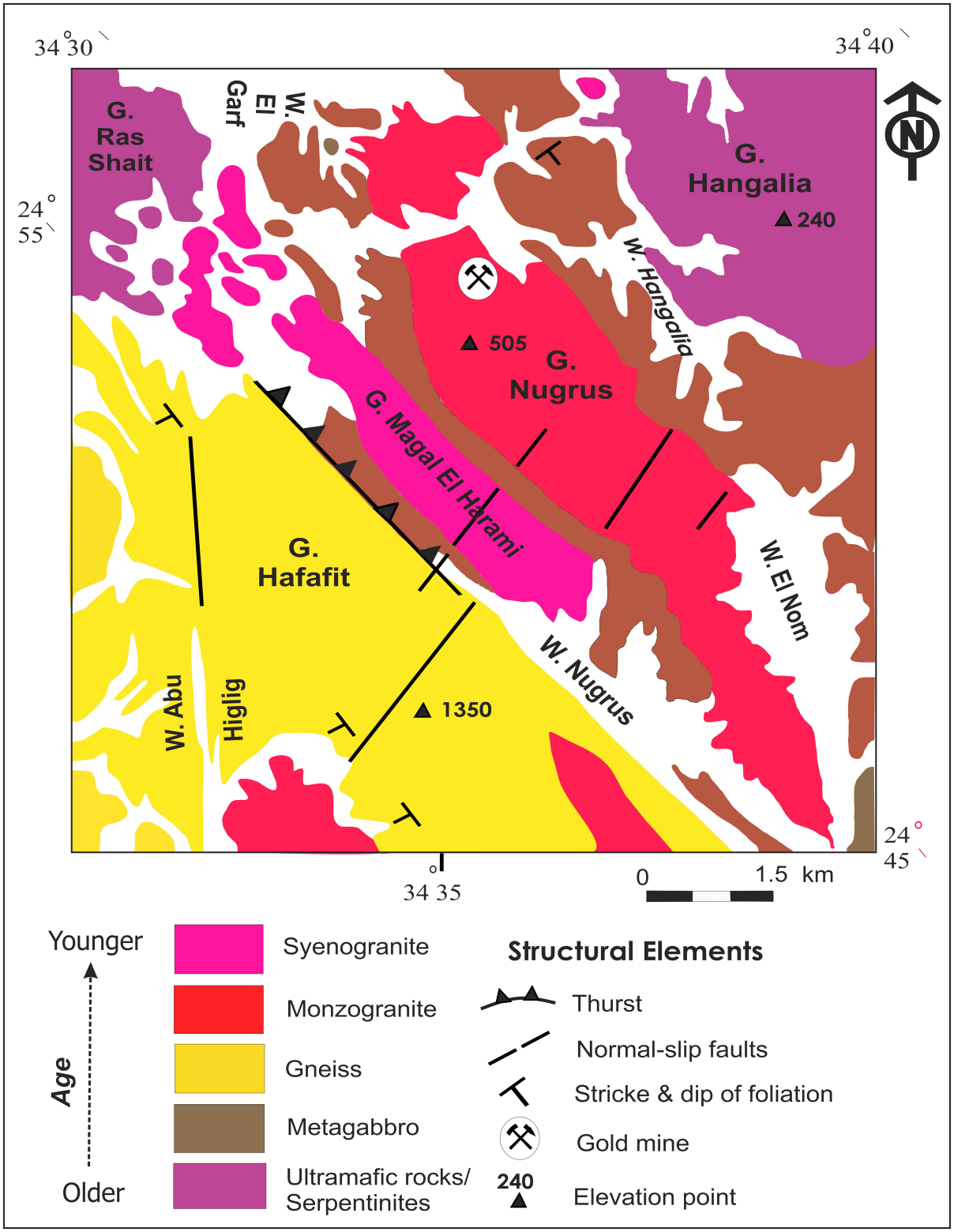


Figure 3

Geological map of Nugrus area, SED, Egypt (modified after Surour et al., 2001).

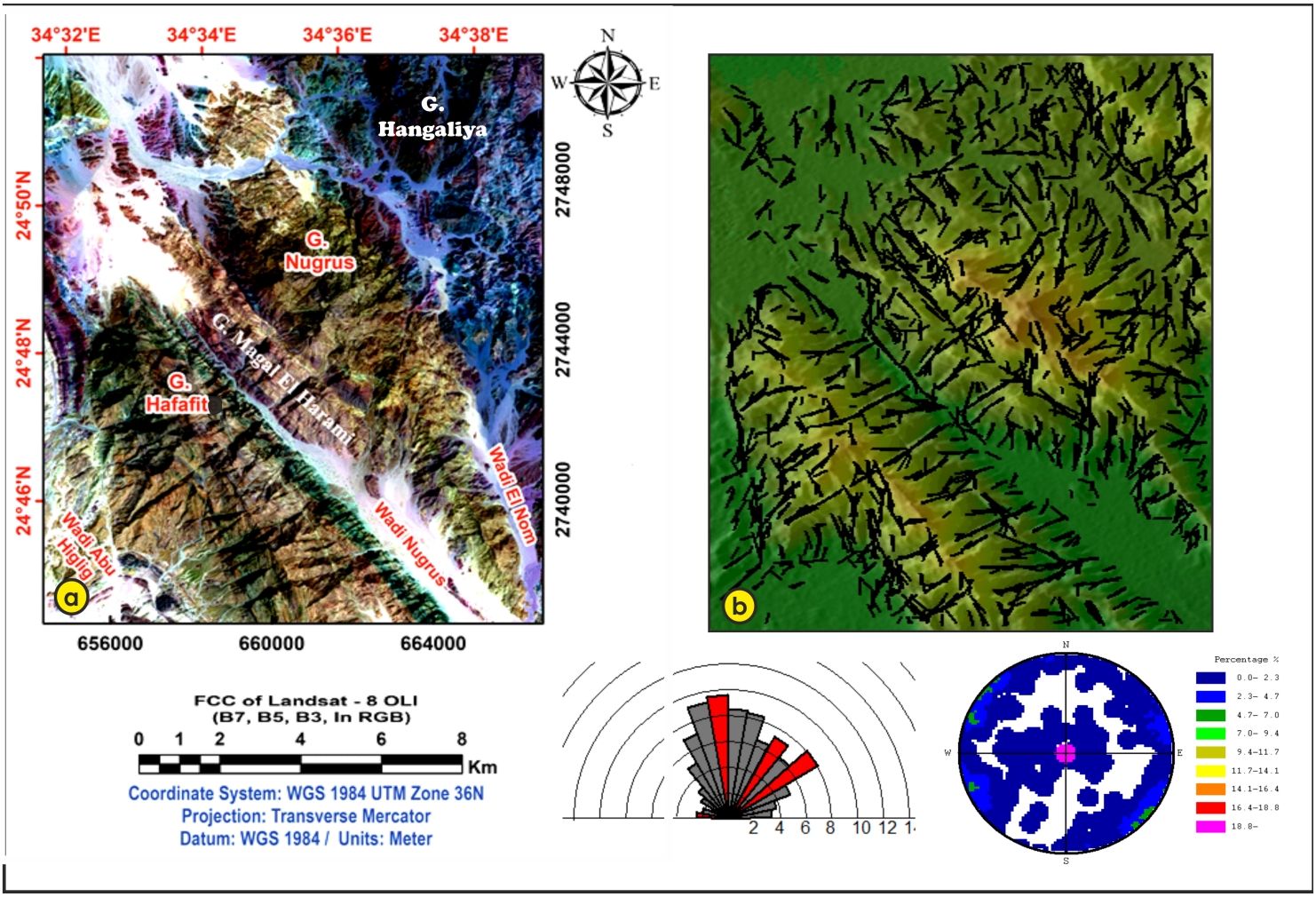


Figure 4

a) False color composite landsat 8 image in RBG of Nugrus area, SED, Egypt. b) Extracted structural patterns in Nugrus area, based on Google Earth and multispectral aerial/satellite images. Rose diagram and lineament density map are included.

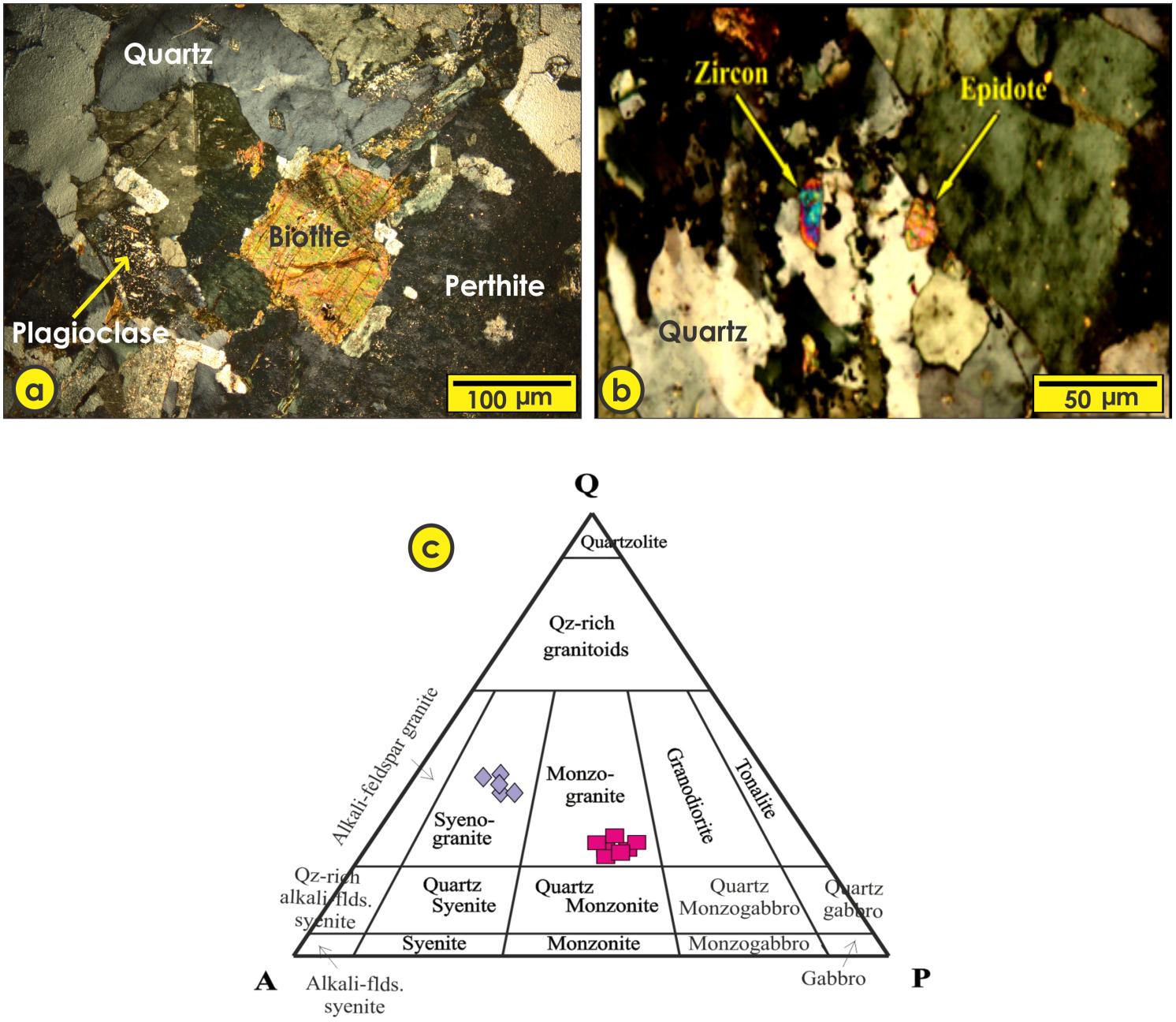


Figure 5

Photomicrograph in crossed polarized light (XPL) of Nugrus area showing: a) Biotite crystals envelop some other accessory minerals, in association with quartz, saussurized plagioclase and perthite in monzogranite at G. Nugrus, b) Equigranular texture in syenogranite rock showing epidote and zircon crystals enveloped within quartz grains at Magal El Haram pluton, and c) Modal composition for the studied granitoids on the QAP ternary diagram (Streckeisen, 1976).

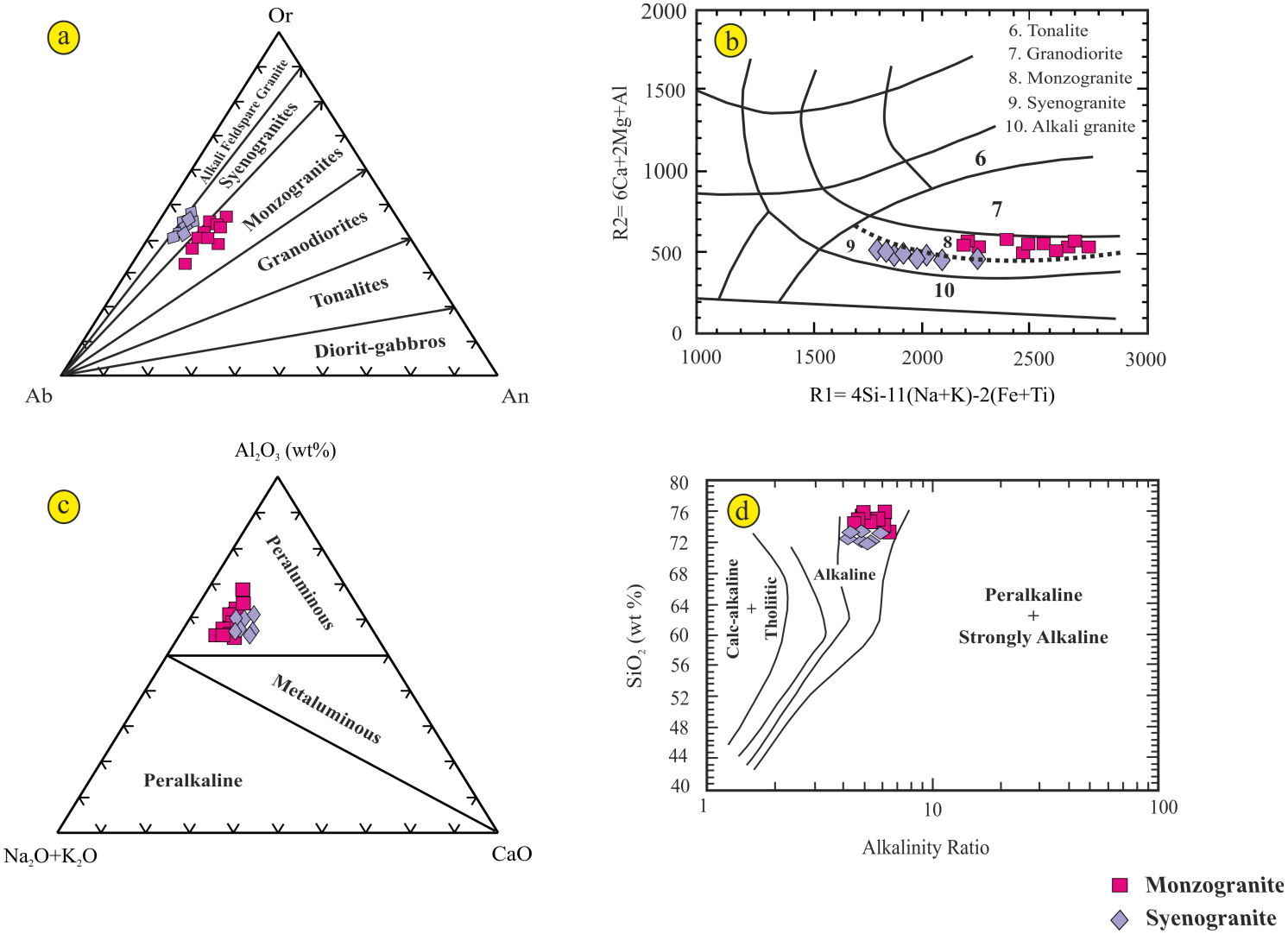


Figure 6

Classification diagrams for the granitic rock at Nugrus area, SED, Egypt.: a) Normative Ab-Or-An ternary diagram for the plutonic rocks ((Streckeisen, 1976), b) R1-R2 binary diagram after (De la Roche et al., 1980). Magma type's discrimination diagrams: c) Al_2O_3-(Na_2O+K_2O)-CaO diagram after (Hermes et al., 1978), d) Alkalinity ratio versus SiO_2 (wt.%) diagram for the studied granitic rocks after (Wright, 1969).

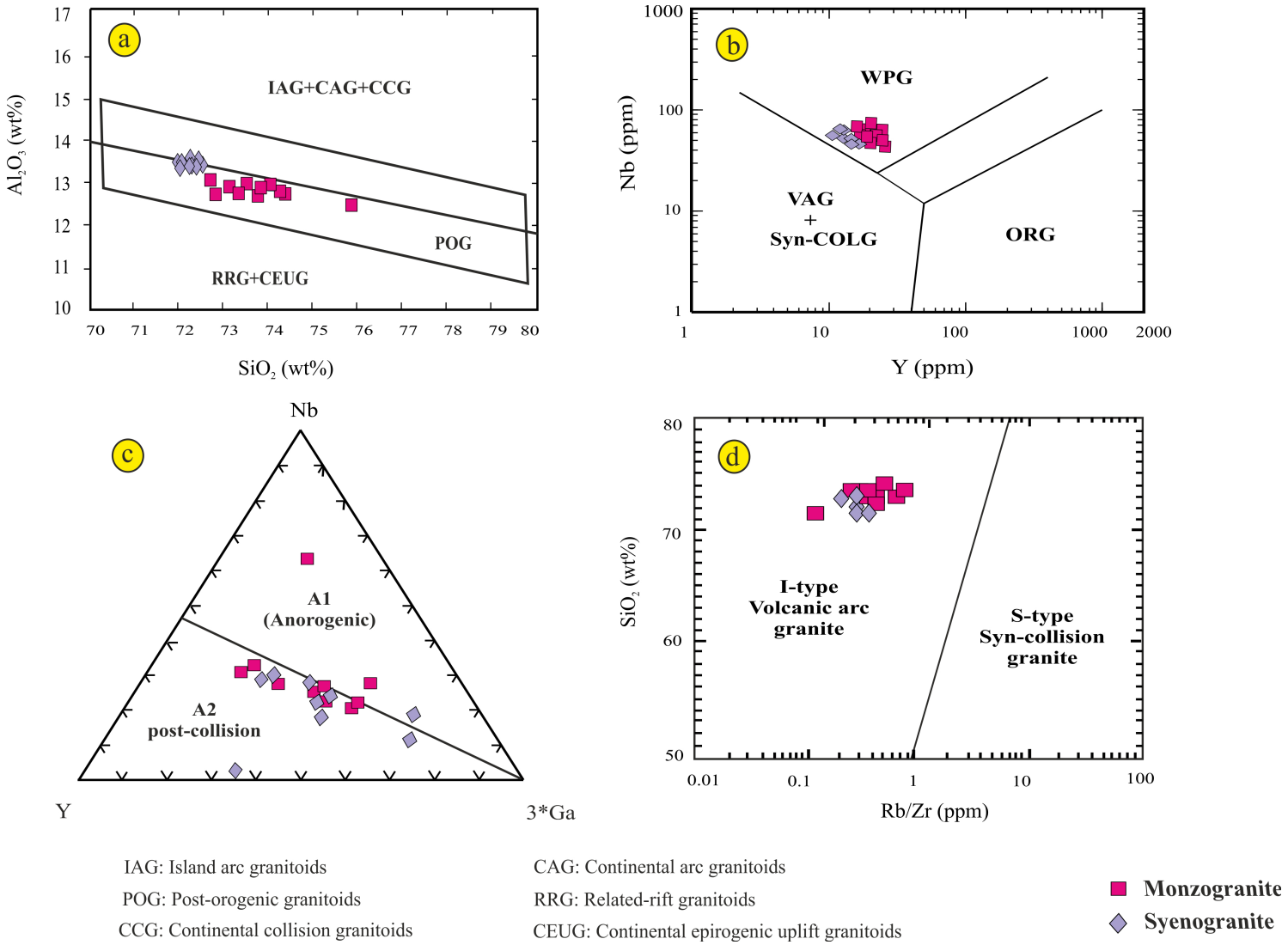


Figure 7

Tectonic settings for the studied granitoids at Nugrus area, SED, Egypt: a) SiO_2 (wt.%) versus Al_2O_3 (wt.%) diagram after (Maniar and Piccoli, 1989), b) Plots on Nb-Y (ppm) diagram after (Pearce et al., 1984), c) Y-Nb-3*Ga (ppm) discrimination diagram of Eby (1992), and d) SiO_2 (wt.%) versus Rb/Zr (ppm) binary diagram after (Harries et al., 1986).



Figure 8

Field photographs at Hangaliya gold mine showing: a) Hangaliya granitic pluton with referring to ancient ruins, buildings and old mining track, b) Inclined shaft driven into Hangaliya gold mine, c) Ancient grinding stone indicating historical gold processing, d) Auriferous quartz veinlets with noticeable supergene alteration, and e) Visible pyrite cubes within the rock adjacent to the mineralized quartz veins.



Figure 9

Detailed geologic map for the Hangaliya gold mine.

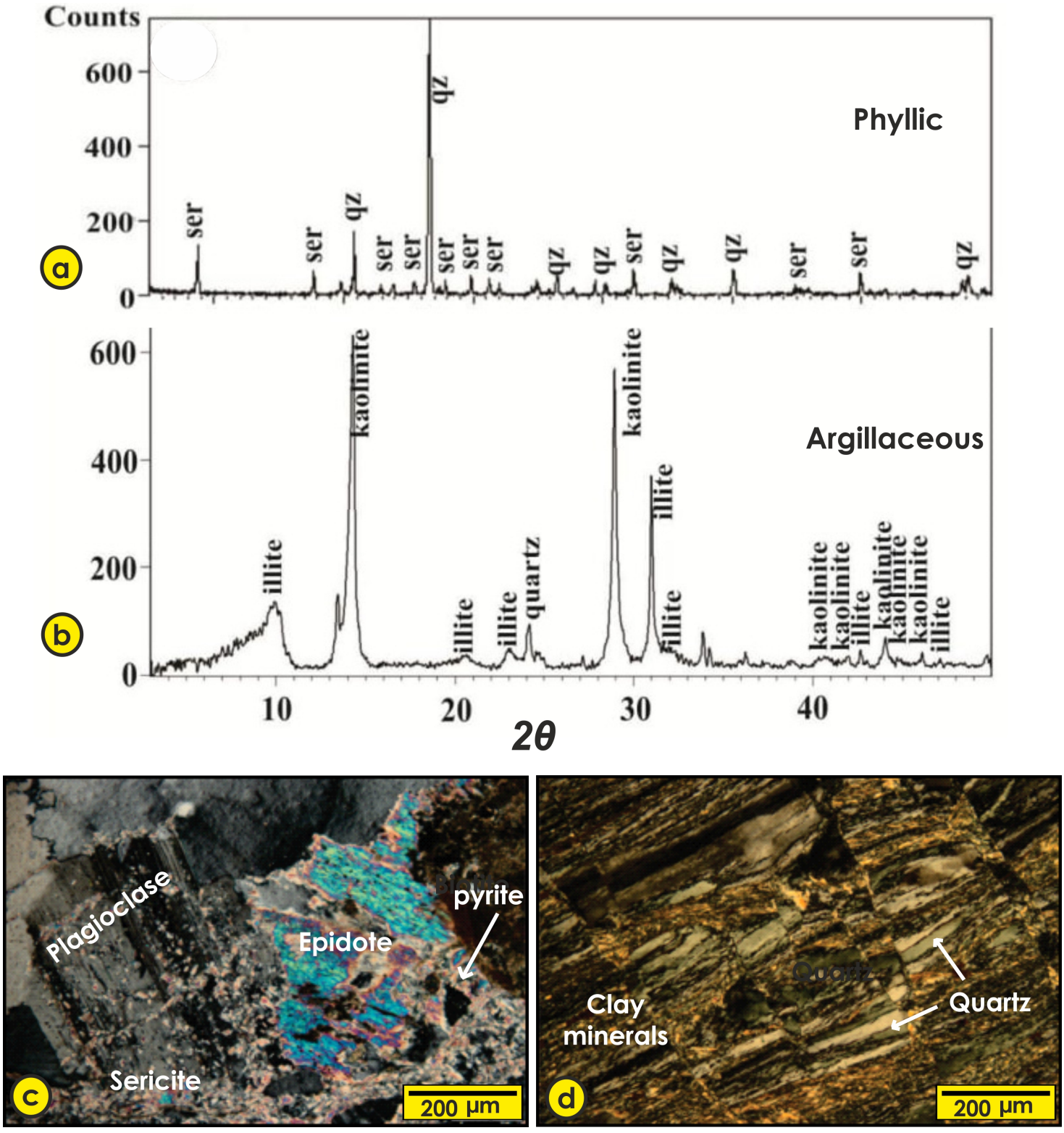


Figure 10

a) XRD chart from the phyllic alteration zone (ser=sericite, qz=quartz), b) XRD chart from the argillaceous alteration zone. Photomicrographs in crossed-polarized light (XPL) showing: c) Sericite, epidote, and pyrite in the phyllic alteration type, d) Clay minerals intercalated with quartz grains in from the argillaceous alteration type.

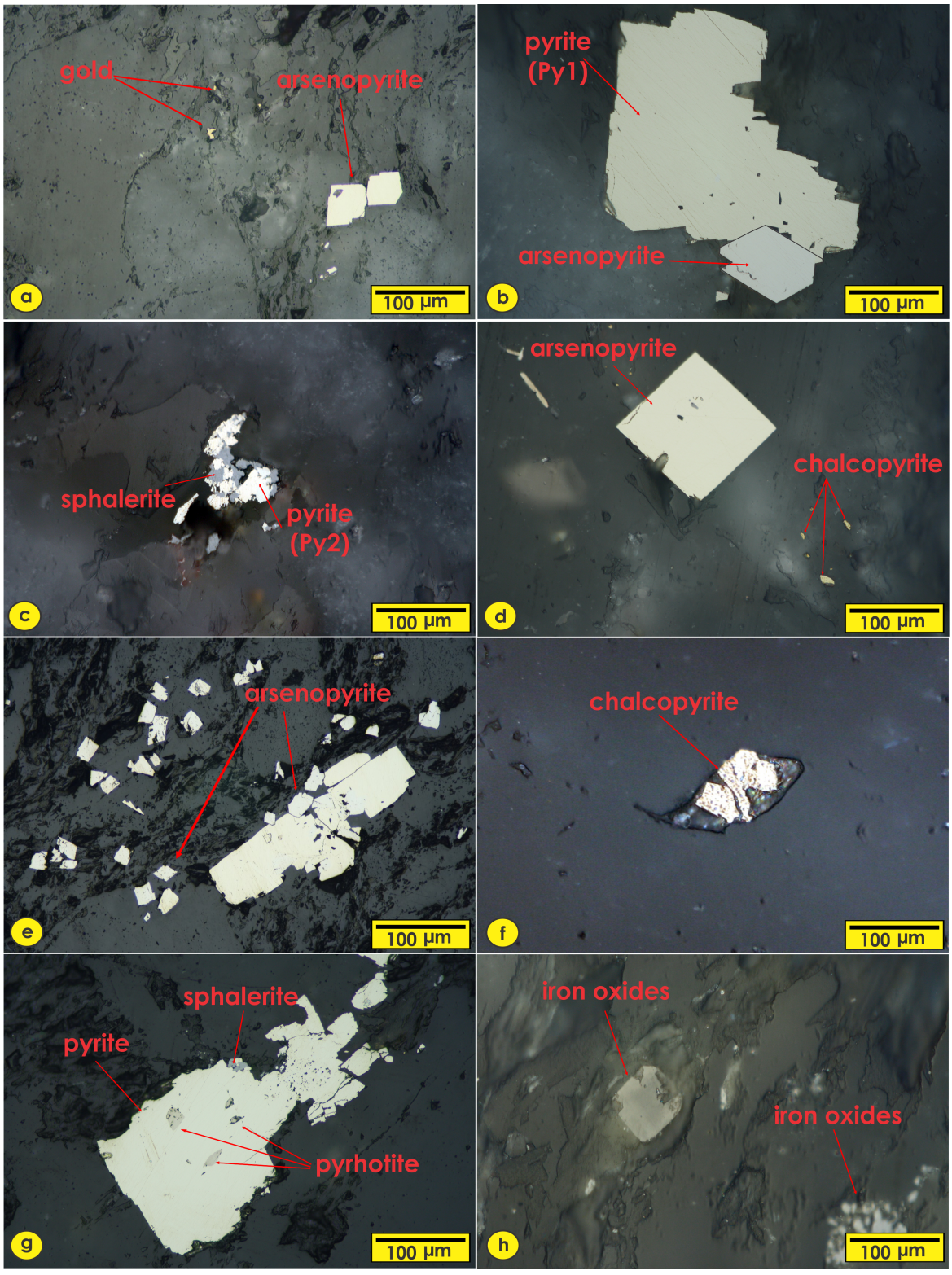


Figure 11

Photomicrograph in reflected light (RL) from the mineralized quartz veins at Hangaliya gold deposits showing: a) Minute grains of gold scattered in the quartz vein nearby arsenopyrite, b) Coarse-grained crystals (Py1) attached with idiomorphic arsenopyrite, c) Medium-grained pyrite (Py2) in association with sphalerite, d) Rhombic-shaped arsenopyrite grain associated with chalcopyrite, e) Medium-grained, euhedral arsenopyrite crystals scattered within the quartz groundmass, f) Partial alteration of

chalcopyrite crystal giving rise to covellite, g) Fine anhedral aggregates of pyrrhotite included within large pyrite, and h) Scattered goethite grains represent an alteration product for previously-formed iron oxides and/or pyrites.

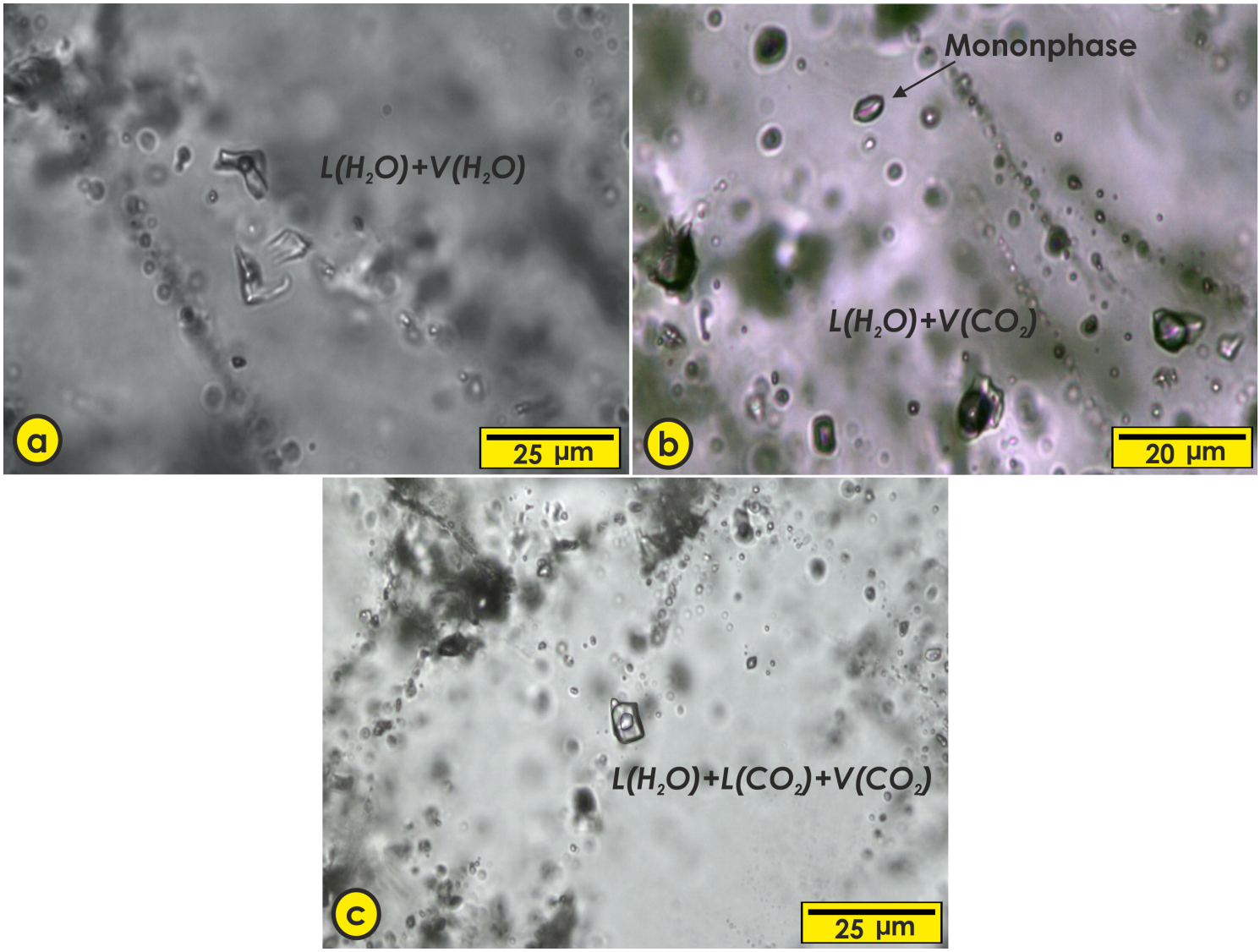


Figure 12

Photomicrographs for fluid inclusions (FIs) from the mineralized quartz veins at Hangaliya gold deposits showing: a) Two-phases aqueous FIs of primary nature, b) Two-phases aqueous-carbonic FIs, with refereeing to monophase inclusions, and c) Three-phase of mixed aqueous-carbonic FIs.

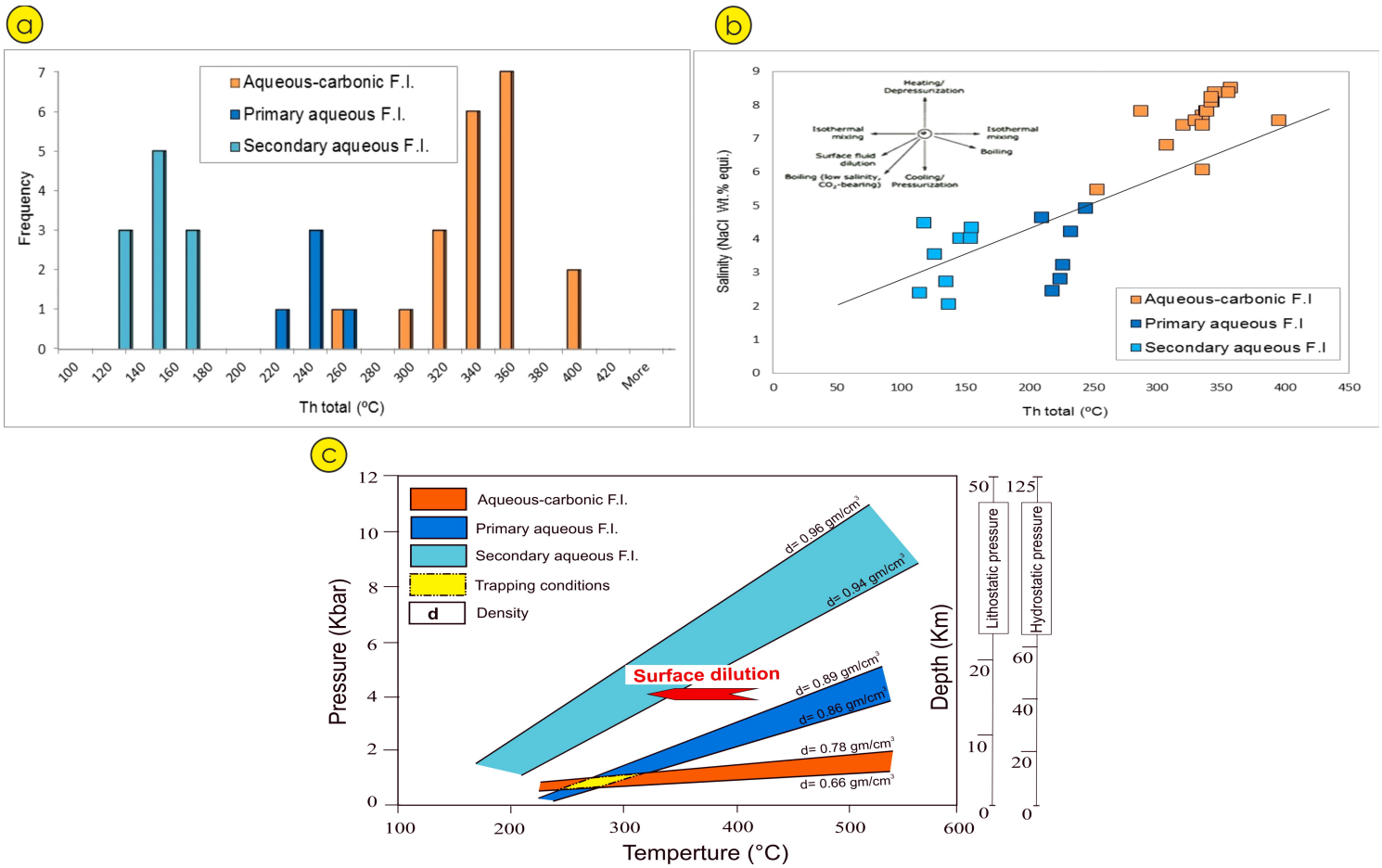


Figure 13

a) Frequency histogram for the distribution of the total homogenization temperatures (Th total) (°C) in Hangaliya gold deposits, b) Binary relationship diagram between a) salinity (wt.% NaCl equi.) and (Th total) (°C) after (Wilkinson, 2001) in Hangaliya gold deposits, and c) Combined isochores construction for various densities of different FIs types at Hangaliya gold deposits. Lithostatic and hydrostatic depths were calculated in suppose of average SP.G. for granite as 2.7 g/cm³. The curved line separating between single and two-phases FIs based upon the fluid composition of (H_2O+4.5 wt.% NaCl equi.+10 mol.% CO_2) (Gehrig, 1980).

Supplementary Files

This is a list of supplementary files associated with this preprint. Click to download.

- Tables14.docx